Research Article | Vol. 29, No. 26 / 20 Dec 2021 / Optics Express 42800
Optics EXPRESS

In-situ adjustable fiber-optic piezometer based on parallelly structured external Fabry-Perot interferometers with Vernier effect and its harmonics

SHUN WANG,[1,2] YAOWEN YANG,[1,6] LEI WU,[3,7] LIPI MOHANTY,[1] RUI-BO JIN,[2] LIANG ZHANG,[4] AND PEIXIANG LU[5]

[1]School of Civil and Environmental Engineering, Nanyang Technological University, 50 Nanyang Avenue, 639798, Singapore
[2]Hubei Key Laboratory of Optical Information and Pattern Recognition, Wuhan Institute of Technology, Wuhan 430205, China
[3]School of Petroleum Engineering, China University of Petroleum (East China), Qingdao, 266580, China
[4]Shenzhen Institutes of Advanced Technology, Chinese Academy of Sciences, Shenzhen 518055, China
[5]School of Physics and Wuhan National Laboratory for Optoelectronics, Huazhong University of Science and Technology, Wuhan 430074, China
[6]cywyang@ntu.edu.sg
[7]wulei@upc.edu.cn

Abstract: Translating interferometric applications into practical field use with the required flexible precision and measurement range, is a recognized challenge. We report an in-situ adjustable fiber-optic piezometer based on parallelly structured external Fabry-Perot interferometers (EFPIs) with the Vernier effect and its harmonics. By accommodating the EFPI structure with an adjustable and a fixed cavity length, the EFPIs are utilized as a referencing fiber piezometer (RFP), and a sensing fiber piezometer (SFP), respectively. The Vernier effect with amplified sensitivity is formed by connecting the RFP and SFP in parallel via a 3 dB optical coupler. By simply tuning the cavity length of the RFP, the magnification factor M of the Vernier effect is in-situ continuously adjustable. Using the two prototypes SFP1 and SFP2, water level measurement is performed in the fundamental Vernier effect (FVE) mode and the harmonic Vernier effect (HVE) mode. Experimental results demonstrate that in the FVE mode, the sensitivity can be predictably tuned from −0.15 nm/cm to −7.02 nm/cm with M=1~48 for SFP1, and −0.31 nm/cm to −7.22 nm/cm with M=1~23 for SFP2. In the HVE mode, the sensitivity can be further enhanced as high as −9.08 nm/cm, while the sensing performance fluctuates during the adjusting process. Benefiting from the merits of in-situ adjustable sensitivity and measurement range, simplicity of composition, robustness, and remote sensing capability, the proposed scheme can be applied to various practical applications.

1. Introduction

Piezometers are geotechnical sensors that are used to measure pore water pressure (PWP) in the soil, earth/rock fills, foundations, and concrete structures [1]. In the last decades, piezometers have been widely used in construction control, stability investigation, shallow underground works [2], groundwater pressure study [3] and monitoring of slope failure [4], landslides [5], earth dams [6], embankments [7], etc. As compared with traditional electrical piezometers [8,9], the unique advantages of optical fiber-based piezometers such as immune to electromagnetic interference (EMI) and their multiplexing potential bring them widespread attention [10,11]. Among them, the FBG and interference-based piezometers [12,13] are two typical representatives,

#445192 https://doi.org/10.1364/OE.445192
Journal © 2021 Received 6 Oct 2021; revised 15 Nov 2021; accepted 30 Nov 2021; published 8 Dec 2021

Optics EXPRESS

showing stable and reliable characteristics. However, their performance in terms of sensitivity or resolution can be further improved.

The Vernier effect, firstly used in a Vernier caliper, can significantly enhance detection accuracy and is widely used in many measurement fields by utilizing the overlapping effect of two scales [14]. In recent years, the Vernier effect has been employed in optical fiber sensing technology, in which two interferometers are connected in cascade or parallel structures [15]. These two interferometers can be the same such as the Mach-Zehnder interferometers (MZIs) [16], Michelson interferometers (MIs) [17], Sagnac interferometer (SIs) [18], Fabry-Perot interferometers (FPIs) [19], microfiber knot resonators (MKRs) [20], fiber couplers [21], or combinations of any two of them [22–25]. Due to its magnification mechanism, the Vernier effect appears to be a promising solution for sensing applications with real-time controllable performance. Xu et al. [26] proposed a sensitivity-controllable refractive index sensor based on a reflective θ-shaped microfiber resonator that cooperated with the Vernier effect. However, the sensing structure is difficult to manufacture, and its adjustment is not conducive to practical applications. Wang et al. [27] proposed an ultra-sensitive gas pressure sensor based on the Vernier effect with a controllable amplification factor, but it is difficult to achieve continuous adjustment on-site based on their femtosecond processing and splicing manufacturing process. For practical applications, an in-situ continuously adjustable fiber-optic sensor based on the Vernier effect is desired, which has yet been reported in literature.

The harmonic Vernier effect (HVE) [28–30], different from the slight optical path difference between two interferometers in the fundamental Vernier effect (FVE), has multiple relationships between the optical path differences of interferometers. Based on the HVE method, Gomes et al. [31] achieved a giant refractometric sensitivity (a magnification factor over 850) by combining the extreme optical Vernier effect and modal interference, further amplifying the detectable range compared with the FVE method.

In this article, an in-situ adjustable fiber-optic piezometer based on a parallelly structured EFPI with both the FVE and HVE is theoretically and experimentally demonstrated. The EFPI is simply formed by a fiber ferrule connector/flat contact (FC/FC) connector and an aluminum foil pasted on a thin metal plate. When accommodating the EFPI structure, a referencing fiber piezometer (RFP) and a sensing fiber piezometer (SFP) are formed by using an adjustable and a fixed cavity length, respectively. By connecting the RFP and SFP in parallel, the Vernier effect with amplified sensitivity is formed. By simply tuning the cavity length of the RFP, the magnification factor M of the Vernier effect is in-situ continuously adjustable. Since the RFP is not used for measurement (e.g. installed in a borehole or pressure chamber), tuning of its cavity length can be done on spot thus achieving an in-situ adjustment of sensor sensitivity. A water level measurement is carried out in both the FVE and HVE modes on two prototypes SFP1 and SFP2. In the FVE mode, the sensitivity can be predictably tuned from −0.15 nm/cm to −7.02 nm/cm with M=1~48 for SFP1, and −0.31 nm/cm to −7.22 nm/cm with M=1~23 for SFP2. In the HVE mode, the sensitivity can be further enhanced up to −9.08 nm/cm but with a fluctuated performance during the adjusting process. In addition, the advantages of the proposed scheme such as in-situ adjustable sensitivity, tunable working range, simplicity of composition, robustness, and remote sensing capability, further facilitate its potential for practical applications.

2. Experimental setup and principle

2.1. Single EFPI

The schematic of the EFPI structure with air cavity is shown in Fig. 1, which is simply formed by an FC/FC connector and a piece of aluminum foil (99.99% purity, 20 μm thickness, 3 mm diameter) pasted on a circular metal plate (0.75 mm thickness, 15 mm radius). The entire optical structure is well protected and accommodated by a cylindrical component made of aluminum alloy. One physical piezometer prototype as a reference interferometer is also shown in Fig. 1,

Optics EXPRESS

indicating its compact and robust characteristics. It is worth noting that the components of the air cavity are connected by fine threads, enabling its adjustment function of the RFP. In other words, the cavity length and the free spectrum range (FSR) of the RFP can be adjusted in real-time by rotating the threaded part as needed. In addition, it would be good for miniaturization and adaptation of fiber piezometer by integrating the sensing head into a single fiber structure, the easily available components in our case make the sensing structure simple, low-cost, robust, durable and benefit its practical applications.

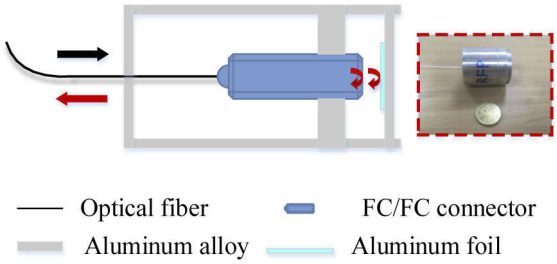

Fig. 1. Schematic diagram of EFPI structure and one prototype of the EFPI piezometer as reference interferometer.

In Fig. 1, the incident beam and the reflected beams are represented by a black arrow and red arrows, respectively. The reflected beams will recombine in the fiber, resulting in a typical interference fringe pattern as output. For a typical EFPI of either the RFP or the SFP, the output intensity can be expressed as [32]:

$$I = I_1 + I_2 + 2\sqrt{I_1 I_2}\cos(\phi_{FP} + \phi_0), \tag{1}$$

where I_1 and I_2 are the light intensities of the reflected beams by the interfaces of the FC/FC connector and the aluminum foil, respectively, ϕ_0 is the initial phase of the EFPI; and ϕ_{FP} is the phase difference of the two reflected light beams. Assuming ϕ_0=0, the resonant wavelength would satisfy the phase condition as [22]:

$$\phi_{FP} = \frac{2\pi * 2L}{\lambda_m} = 2m\pi, \tag{2}$$

$$\lambda_m = \frac{2L}{m}, \tag{3}$$

where for a peak wavelength, the interference order $m = k$; for a dip wavelength, $m = (2k + 1)/2$; and k is a positive integer. L is the cavity length of the EFPI. The FSR of the interference fringe of the EFPI can be given by [33,34]

$$FSR_{FP} = \lambda_m - \lambda_{m+1} = \frac{\lambda_m \cdot \lambda_{m+1}}{2L} \approx \frac{\lambda^2}{2L}. \tag{4}$$

The observed wavelength variation relative to the cavity length variation induced by external pressure can be expressed as

$$\Delta\lambda_{\mathrm{m}} = \frac{\lambda_{\mathrm{m}}}{L_0}\frac{dL}{dP}\Delta P, \tag{5}$$

where L_0 is the initial cavity length of the EFPI.

Optics EXPRESS

2.2. Parallel structured EFPI

Based on the principle and physical prototypes of the single EFPI, the parallel structured EFPI is constructed as shown in Fig. 2, in which the RFP prototype and the SFP prototype are connected in parallel through a 3 dB optical coupler. An interrogator (Miron Optics Si255 1460~1620 nm, 1 pm resolution) is used to illuminate the optical path and collect spectral data. The collected data are processed and displayed on a computer.

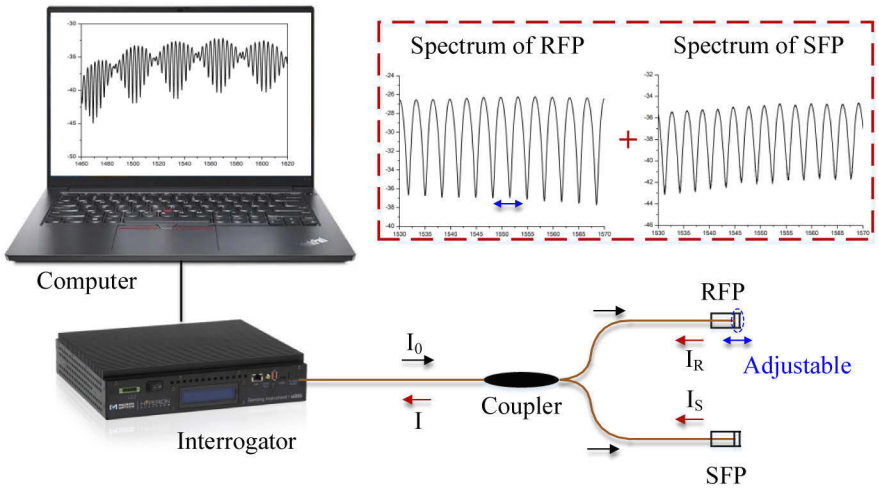

Fig. 2. Schematic diagram of parallel structured EFPI.

As described above, the RFP has an adjustment function on the cavity length, i.e., the FSR of the interference fringe of the RFP is adjustable by tuning the fine threads. Thus, the spectra of the RFP and the SFP with similar but slightly different FSRs can be easily acquired as shown in the dashed red box in Fig. 2. The total transmission spectrum from the superimposition of the two individual fiber piezometers is displayed on the computer. The light intensity of the total transmission can be expressed as [35]

$$I = I_R + I_S \approx A + B\cos\frac{\phi_{RFP} + \phi_{SFP}}{2}\cos\frac{\phi_{RFP} - \phi_{SFP}}{2}, \tag{6}$$

where I_R and I_S are the reflected light intensities of the RFP and SFP, respectively, $\phi_{RFP} = 4\pi L_R/\lambda$ and $\phi_{SFP} = 4\pi L_S/\lambda$ represent the phase difference of the RFP and the SFP, respectively; L_R and L_S are the cavity lengths of the RFP and the SFP; and A and B are the constants determined by the reflectivity of multiple reflective interfaces of the two EFPIs.

2.3. Fundamental Vernier effect

The concept of the Vernier effect comes from the caliper which has two rulers with a slight scale difference. Similarly, by adjusting the cavity length of the RFP to be slightly different from that of the SFP, the optical Vernier effect can be readily achieved. The transmission dips will overlap again after several orders, which leads to a periodic envelope in the Vernier-effect spectrum. As observed in Fig. 2, the Vernier-effect spectrum consists of a series of fringes with different amplitudes in a periodic envelope trend. The FSR of the Vernier-effect envelope can be described as [36,37]:

$$FSR_e = \frac{FSR_S FSR_R}{|FSR_S - FSR_R|} = \left|\frac{\lambda_m \lambda_{m+1}}{2(L_S - L_R)}\right|. \tag{7}$$

Optics EXPRESS

As compared to the single SFP, the envelope of the Vernier effect shows sensitivity magnification. The magnification factor M is an important indicator of the Vernier effect, which can be given by two definitions [28,29]. The first one is defined as the magnification ratio from the FSR of the single sensing interferometer to that of the Vernier envelope, expressed as

$$M = \frac{FSR_e}{FSR_S} = \frac{FSR_R}{|FSR_S - FSR_R|} = \left|\frac{L_S}{L_S - L_R}\right|. \tag{8}$$

As shown in Eq. (7) and (8), both the FSRs and the M-factor of the envelope are determined by the cavity lengths of the EFPIs that form the Vernier effect. The other definition of M is related to the sensing performance, which is the magnification ratio from the wavelength shift of the single sensing interferometer to that of the Vernier envelope, expressed as

$$M = \frac{S_{envelope}}{S_{SFP}} = \frac{\Delta\lambda_e}{\Delta\lambda_m}. \tag{9}$$

It is worth noting that, by adjusting the cavity length of the RFP L_R, the FSR of the Vernier envelope and the M-factor can be well controlled and tuned, enabling its adjustable features in-situ. This will be further verified in the experimental part.

2.4. Harmonic Vernier effect

In the above section of the fundamental Vernier effect (FVE), the two interferometers have a slight difference in the optical path, i.e., cavity lengths. However, in the harmonic Vernier effect (HVE), the cavity length of one EFPI is multiples of the other. Based on the HVE, the sensitivity can be further amplified to a significant level as compared to the FVE [28].

Due to the in-situ adjustable function of our proposed RFP and SFP scheme, the HVE structure can be easily obtained. Compared with increasing the cavity length of RFP, reducing the cavity length of RFP is more conducive, as it renders greater spectral contrast and smaller optical loss. Here in the case of spectral output, reducing the cavity length of RFP is equivalent to increasing the cavity length of the SFP. Thus, the optical path length of the SFP is considered to be increased by i-times the cavity length of the RFP ($L_S' = L_S + iL_R$). i is a positive integer defined as the order of the HVE; the HVE degrades to the FVE when $i = 0$. Then the FSR of the SFP can be given follow:

$$FSR_S^i = \left|\frac{\lambda_m\lambda_{m+1}}{2(L_S + iL_R)}\right|. \tag{10}$$

To form a typical Vernier effect spectrum, the FSRs of the two interferometers will overlap at resonant dips when this match condition is satisfied: $FSR_e^i = kFSR_R = [(i+1)k+1]FSR_S^i$, with $k = FSR_S^i/[FSR_R - (i+1)FSR_S^i]$. Therefore, the FSR of the lower envelope can be written in the form of

$$FSR_e^i = \left|\frac{FSR_R FSR_S^i}{FSR_R - (i+1)FSR_S^i}\right|. \tag{11}$$

The FSR of the HVE internal envelope and the corresponding M-factor can be given by [28]

$$FSR_{ie}^i = \left|\frac{(i+1)FSR_R FSR_S^i}{FSR_R - (i+1)FSR_S^i}\right| = (i+1)FSR_e^i, \tag{12}$$

$$M^i = \frac{FSR_{ie}^i}{FSR_S^i} = \left|\frac{(i+1)FSR_R}{FSR_R - (i+1)FSR_S^i}\right| = (i+1)M. \tag{13}$$

It is clear that compared to the FVE, the FSR and sensitivity of the HVE are both increased by a factor of i+1. Thus, the HVE appears to be a promising way to further improve the performance

Optics EXPRESS

of the sensor. However, when i is increased, the slight cavity length difference i.e. $L_S - (i+1)L_R$ between the two EFPIs becomes harder to maintain as compared to the FVE. This will complicate the adjustment process of the magnification factor, which will be demonstrated in the following experimental part.

3. Results and discussion

3.1. Single EFPI

To verify the above theory, two prototypes of the EFPI piezometer, SFP1 and SFP2 are manufactured. Their corresponding output spectra are shown in Fig. 3(a), where the black and red curves represent the spectra of SFP1 and SFP2 with fringe contrasts of 7.5 dB and 25 dB, respectively. It is noted that their FSRs are 3.04 nm and 6.76 nm, which means that according to Eq. (4), the initial cavity lengths are approximately 398 μm and 178 μm, respectively.

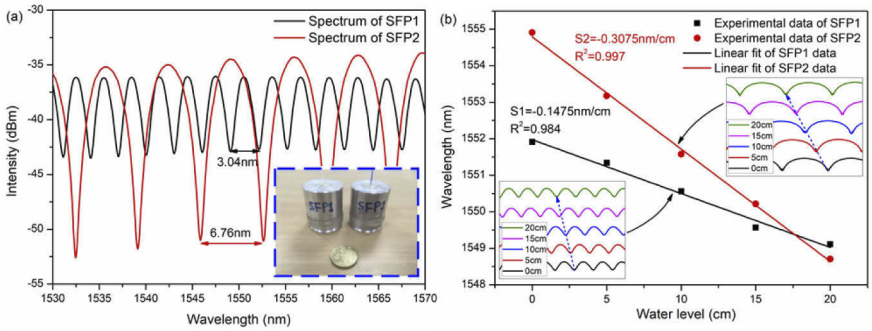

Fig. 3. (a) Initial spectra of sensing fiber piezometers SFP1 and SFP2, (b) Wavelength variation of SFP1 and SFP2 along with water level.

The performance of SFP1 and SFP2 is tested by performing a water level measurement. Their spectrum variations under distinct water levels are shown in Fig. 3(b), in which the spectra are recorded and displayed in vertical offset. As the water level increases from 0 cm to 20 cm in steps of 5 cm, the blue shift process shown by the blue dashed arrows can be observed clearly. The blue shift phenomenon can be explained by Eq. (3) that increasing water pressure reduces the resonant wavelength. The relationships between the wavelength and the water level of SFP1 and SFP2 are also depicted in Fig. 3(b), where the linear fittings reveal their sensitivities of −0.15 nm/cm, and −0.31 nm/cm, respectively.

3.2. Fundamental Vernier effect

The Vernier effect based on two piezometer prototypes SFP1 and SFP2 is demonstrated in a water level measurement with an experimental setup illustrated in Fig. 4. The SFP with fixed cavity length and The RFP with adjustable cavity length as indicated by the blue arrows are connected in parallel configuration through a 3 dB optical coupler. The SFP is immersed in water, and the water level varies from 0 to 20 cm at a step of 5 cm. The corresponding spectra data are collected and recorded by the interrogator. By tuning the cavity length of the RFP, both SFP1 and SFP2 in the FVE and HVE modes are tested in this water level measurement for comparison.

In the FVE mode, a slight cavity length difference between the RFP and the SFP will cause a periodical envelope in the Vernier fringes as shown on the computer screen in Fig. 4. The envelope shifts along with the water level are recorded as shown in Fig. 5(a). The dip of the lower envelope for observation experiences an obvious blue shift as indicated by the dashed blue arrow. The M-factor from FSR can be roughly counted from the envelope fringes, that is, the number of FSR fringes of a single sensing SFP contained in one period of the envelope. Here

Optics EXPRESS

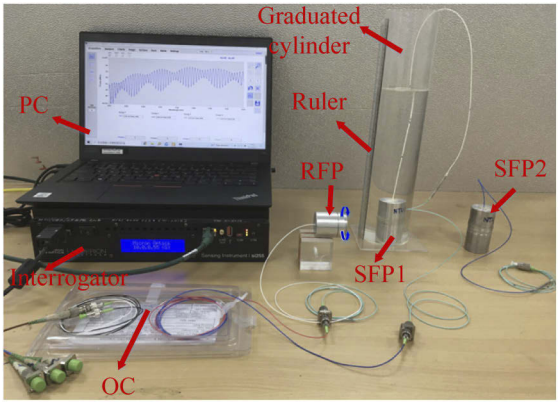

Fig. 4. Experimental setup for water level test.

about 10 fringes are contained as shown by the red lines, implying an M-factor of about 10. The corresponding relationship between the wavelength and the water level is depicted in Fig. 5(b), where the sensing curve of the single SFP1 is also depicted as a comparison. An actual M-factor of 9.56 from measurement sensitivity is acquired, amplifying a sensitivity of −0.15 nm/cm of the single SFP1 to a sensitivity of −1.41 nm/cm of SFP1 in an FVE mode.

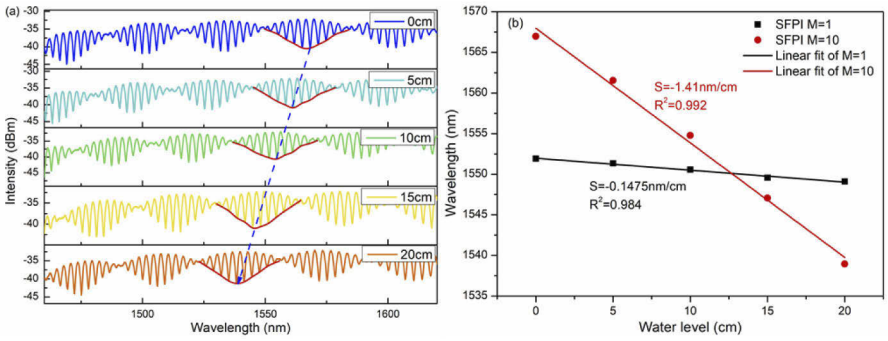

Fig. 5. (a) Spectra under water level test with one vernier structure M=10; (b) Relationship between wavelength and water level compared with that of single SFP1.

By continuously tuning the cavity length of the RFP and counting the FSR fringes in one period of the envelope, the M-factor or measurement sensitivity of the SFP1 in the FVE mode can be well controlled and adjusted. The output spectra are shown in Fig. 6(a), in which the number of the fringe in one period of the envelope or the M-factor is adjusted to be 6, 10, 14, and 48. The corresponding wavelength shifts under these tuned states as a function of the water level are recorded and depicted in Fig. 6(b), where the sensing curve of the single SFP1 is also included for comparison. It reveals that the sensitivity of the single SFP1 (−0.15 nm/cm) is continuously magnified to be −0.82 nm/cm, −1.41 nm/cm, −2.08 nm/cm, and −7.02 nm/cm with corresponding sensing M-factors of 5.59, 9.56, 14.09, and 47.57, respectively. These results indicate that the function of in-situ adjustable sensitivity is realized based on the SFP1 in the FVE mode. However, when the sensitivity is amplified to a large multiple (the green line), the measurement range is narrowed, which is limited by the 160 nm wavelength range of the interrogator.

Optics EXPRESS

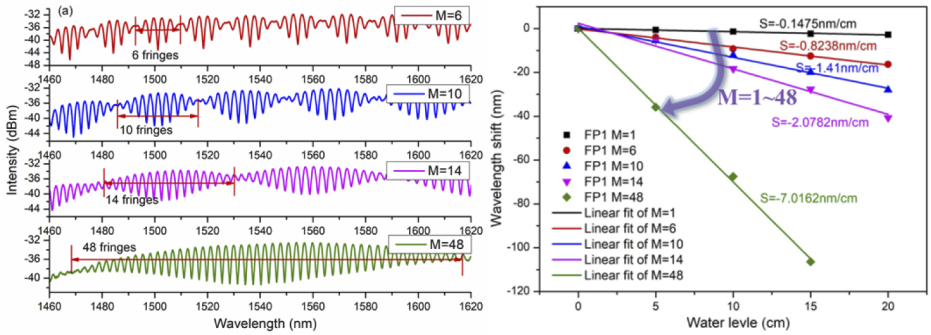

Fig. 6. (a) Vernier spectra of SFP1 with a magnification factor of 6, 10, 14, and 48; (b) Corresponded relationships between the wavelength shifts and the water level.

To further verify the in-situ adjustable function, effectiveness, and repeatability of the proposed scheme in the FVE mode, the same measurement process is repeated on the piezometer prototype SFP2 which has a shorter cavity length. The Vernier spectra with M-factors from FSR continuously adjusted from 4, 9, 13, to 23, are shown in Fig. 7(a). The corresponding sensing curves under these tuning states are depicted in Fig. 7(b), showing the actual sensing M-factors from 3.81, 9.17, 13.07, to 23.48. Similar to the SFP1 in FVE mode, when the sensitivity is amplified to a large multiple, the measurement range becomes narrower as shown by the green line. It should be noted that the sign of sensitivity changes, that is, the negative sensitivity of the single SFP2 becomes positive in the FVE mode. This can be explained by the relationship $L_{SFP2}<L_{RFP}<L_{SFP1}$, so the wavelength shift will undergo a sign change as compared with the SFP1 in the FVE mode.

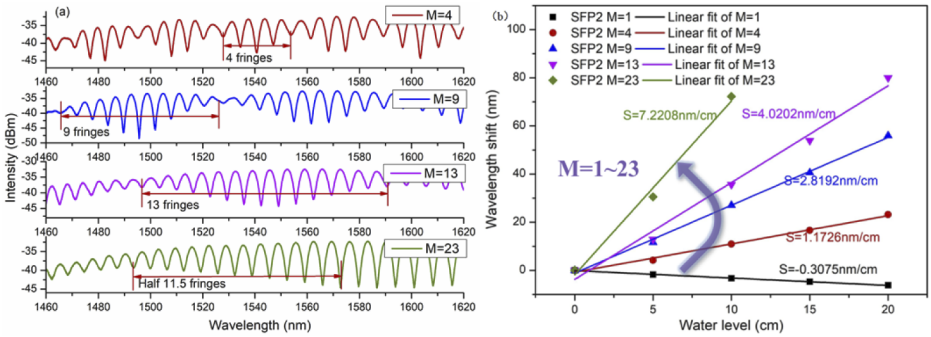

Fig. 7. (a) Vernier spectra of SFP2 with magnification factors of 4, 9, 13, and 23; (b) Corresponding relationships between the wavelength shifts and the water level.

3.3. Harmonic Vernier effect

Based on the HVE, as mentioned before, the sensitivity can be further amplified to a significantly higher level. To verify it, the prototypes SFP1 and SFP2 are also tested in the HVE mode. As shown in Fig. 8(a), the harmonic Vernier spectrum of SFP1 with harmonic order i=1 shows two internal envelopes in red and pink. And the cross point of the two internal envelopes can be the observation point during the measurement as shown in Fig. 8(b), which indicates an obvious blue shift.

By tuning the cavity length of the RFP, the spectra under different harmonic orders i=1, 2, 3 are obtained as shown in Fig. 9(a), including the spectrum in FVE mode (i=0, M=6) for comparison.

Optics EXPRESS

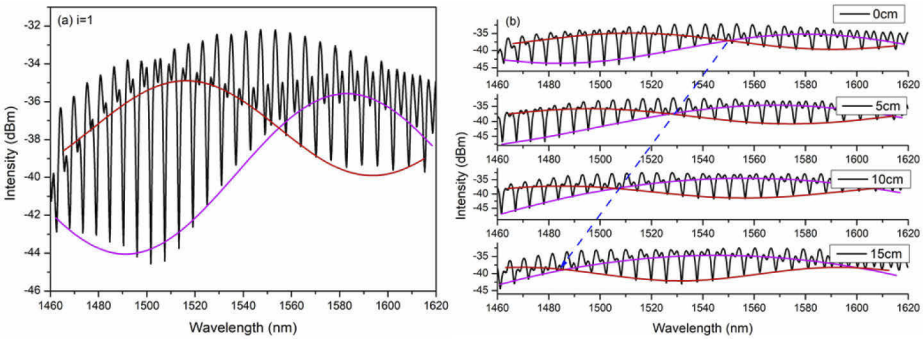

Fig. 8. (a) Harmonic Vernier spectrum of SFP1 with i=1 and (b) corresponding spectra shifts with the water level.

The number of the internal envelopes is equal to i+1. By observing the shift of the cross point, the corresponding sensing curves under i=1, 2, 3 are shown in Fig. 9(b), where the sensitivity is magnified to be −4.38 nm/cm, −9.08 nm/cm, and −2.52 nm/cm. The corresponding M-factors are 29.70, 61.57 and 17.07 as compared to the single SFP1.

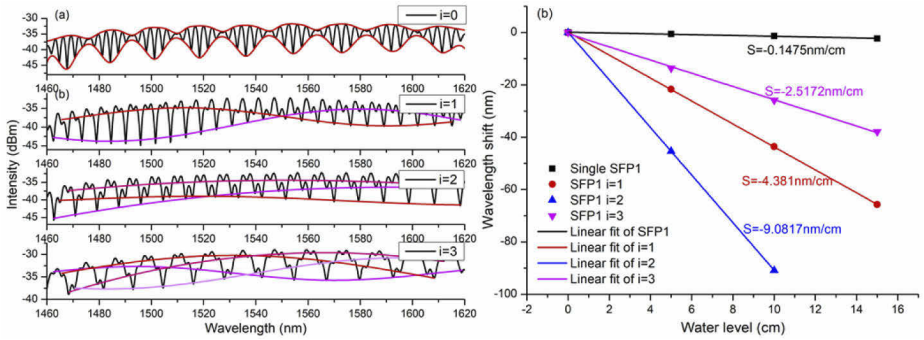

Fig. 9. (a) Harmonic Vernier spectra of SFP1 with i=1, 2, 3, and (b) corresponding sensing curves.

Similarly, SFP2 in the HVE mode is also tested. The spectra under different harmonic orders i=1, 2, 3 are shown in Fig. 10(a), including the spectrum in FVE mode (i=0, M=4) as a comparison. By observing the shift of the cross point, the corresponding sensing curves under i=1, 2, 3 are shown in Fig. 10(b). The sensitivity is magnified to be −7.45 nm/cm, −4.20 nm/cm, and −1.38 nm/cm, with corresponding M-factors of 24.22, 13.65 and 4.48 as compared to the single SFP2, respectively.

Both SFP1 and SFP2 in the HVE mode do not show a continuous increase in sensitivity as expected when the harmonic order changes in integers. This may be attributed to the manual adjustment of the reference states (tuning the fine threads) in the FVE mode. It can be improved by using a more sophisticated adjustment apparatus but sacrificing the cost-effectiveness and simplicity of the system at the same time. Nevertheless, SFP1 and SFP2 in the HVE modes still show further magnified sensitivities up to −9.08 nm/cm and −7.45 nm/cm, respectively, as compared to the FVE mode.

3.4. Performance comparison

The performance comparison of the above-mentioned demodulation schemes (single SFP, SFP in FVE mode, SFP in HVE mode) is listed in Table 1, in terms of the sensitivity, resolution, M-factor

Optics EXPRESS

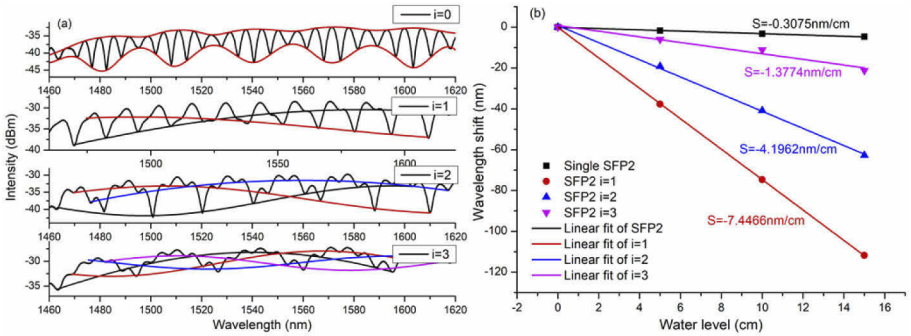

Fig. 10. (a) Harmonic Vernier spectra of SFP2 with i=1, 2, 3, and (b) corresponding sensing curves.

by FSR, M-factor by sensitivities and measurement range. Compared with the single SFP with fixed sensitivity, both the FVE mode and HVE mode show obvious magnification on sensitivity, showing ~μm level water level sensing resolution. Sensing structure in the HVE mode further enhances the performance as compared to the FVE mode. For in-situ continuous adjustment, the FVE mode shows better controllability on the sensing M-factor, and the HVE mode does not show a consistent increase on the sensing M-factor. It is worth noting that the sensor resolution values listed in the table are derived from the ratio of instrument's demodulation resolution to sensor sensitivity, which is only used as an index for comparison. In practical applications, the sensing error would increase along with the enhancement of sensitivity. The actual measurement resolution would be affected by the noise floor induced by the external environment and reading error from data processing.

Table 1. Performance Comparison of Demodulation Schemes

Method	Item	Test	Sensitivity (nm/cm)	Resolution (mm)	M by FSR (or fringes)	M by Sensitivities	Range (cm)	Sensitivity predictable
Single FP	SFP1	#1	−0.1475	0.068	1	1	1085	Fixed
	SFP2	#1	−0.3075	0.033	1	1	520	
Fundamental Vernier effect	SFP1	#1	−0.8238	0.012	6	5.86	194	Predictable and adjustable on M-factor
		#2	−1.41	0.007	10	9.56	113	
		#3	−2.0782	0.005	14	14.09	77	
		#4	−7.0162	0.001	48	47.57	23	
	SFP2	#1	1.1726	0.009	4	3.81	136	
		#2	2.8192	0.004	9	9.17	57	
		#3	4.0202	0.002	13	13.07	40	
		#4	7.2208	0.001	23	23.48	22	
Harmonic Vernier effect	SFP1	i=1	−4.381	0.002	–	29.70	37	Amplified but fluctuated on M-factor
		i=2	−9.0817	0.001	–	61.57	18	
		i=3	−2.5172	0.004	–	17.07	64	
	SFP2	i=1	−7.4466	0.001	–	24.22	21	
		i=2	−4.1962	0.002	–	13.65	38	
		i=3	−1.3774	0.007	–	4.48	116	

Optics EXPRESS

Besides, limited by the wavelength range of the interrogator, the measurement range of the proposed schemes is inversely proportional to measurement sensitivity. In fact, the measurement range can be expanded by adopting a widened wavelength range of the interrogator or OSA, but this will also increase the system cost. To clarify the variation trends of these two important performance indicators, their numerical changes are represented by the histogram shown in Fig. 11. The results of SFP1 in the single sensing mode, FVE mode and HVE mode are shown in Fig. 11(a), and those of SFP2 are shown in Fig. 11(b). Their sensitivities are indicated in the black color while measurement range in red, and the corresponding arrows show their adjustment process. As demonstrated, compared with the single SFP, the measurement sensitivity can be significantly magnified in both the FVE and HVE modes. The FVE mode shows continuously adjustable performance, while the HVE mode shows fluctuation in performance with the tuning process despite that it can achieve higher sensitivity. Besides, the variation trend of the measurement range shows the completely opposite trend as compared with that of the sensitivity.

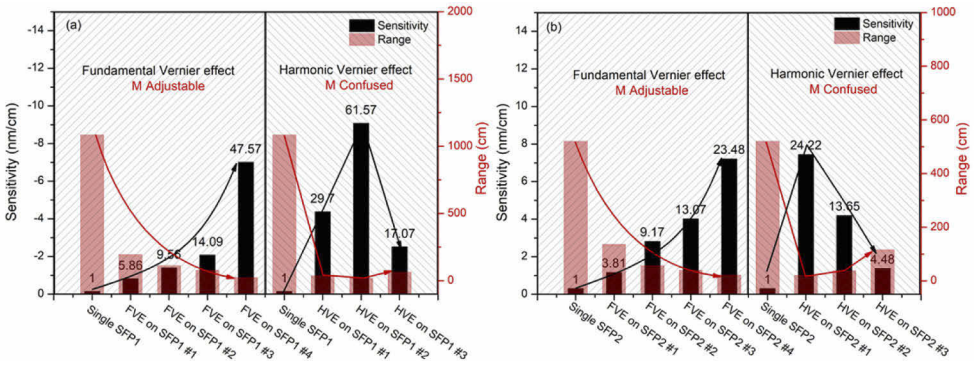

Fig. 11. Performance comparison between FVE and HVE of proposed piezometer.

4. Conclusion

In summary, we theoretically and experimentally demonstrated an in-situ adjustable fiber-optic piezometer based on a parallelly structured EFPIs by utilizing the Vernier effect. By simply adjusting the cavity length of the RFP, a water level measurement is performed in both the FVE and HVE modes using prototypes SFP1 and SFP2. In the FVE mode, the sensitivity can be predictably tuned from −0.15 nm/cm to −7.02 nm/cm with magnification factor M from 1 to 48 for SFP1, and −0.31 nm/cm to −7.22 nm/cm with M from 1 to 23 for SFP2. In the HVE mode, the sensitivity can be further enhanced up to −9.08 nm/cm but with an inconsistent performance with the adjustment process as compared to the FVE mode. Moreover, the device is featured with in-situ adjustable sensitivity, tunable measurement range, simplicity of composition, robustness, and remote sensing capability, which make it attractive in various practical applications.

Funding. National Natural Science Foundation of China (12104350); Science and Engineering Research Council (1992200001); Taishan Scholar Project of Shandong Province (tsqn201909067).

Disclosures. The authors declare no conflicts of interest.

Data availability. Data underlying the results presented in this paper are not publicly available at this time but may be obtained from the authors upon reasonable request.

References

1. A. J. Mazur, L. M. Schouten, W. Y. Lam, and P. H. Setiawan, "Nude vibrating wire piezometer installations-no filter response zone and no engineered grout," in *Proceedings of the Ninth Symposium on Field Measurements in Geomechanics, Australian Centre for Geomechanics*, (Academic, 2015), pp. 487–500.

Optics EXPRESS

2. J. Zhao, J. Chen, X. Zhang, J. Ning, and Y. Zhang, "Distribution characteristics of floor pore water pressure based on similarity simulation experiments," Bull. Eng. Geol. Environ. **79**(9), 4805–4816 (2020).
3. M. M. Nistor, H. Rahardjo, A. Satyanaga, K. Z. Hao, Q. Xiaosheng, and A. W. L. Sham, "Investigation of groundwater table distribution using borehole piezometer data interpolation: Case study of Singapore," Eng. Geol. **271**, 105590 (2020).
4. S. Chaulya and G. M. Prasad, *Sensing and monitoring technologies for mines and hazardous areas: monitoring and prediction technologies* (Elsevier, 2016).
5. C. Zet, C. Foşalău, and D. Petrişor, "Pore water pressure sensor for landslide prediction," IEEE Sens. J. 1–4 (2015).
6. M Dilawari, *Forecasting models for the displacements and the piezometer levels in a concrete arch dam* (McGill University, 2018).
7. I. S. Jung, *Anomaly Detection of Piezometer Data Collected from Embankment Dams* (Carnegie Mellon University, 2015).
8. C. N. Dourado, *Characterizing Aquitard Properties from the response of Grouted Vibrating Wire Piezometers to Surface Loading* (University of Saskatchewan, 2018).
9. A. J. Merritt, J. E. Chambers, W. Murphy, P. B. Wilkinson, L. J. West, S. Uhlemann, P. I. Meldrum, and D. Gunn, "Landslide activation behaviour illuminated by electrical resistance monitoring," Earth Sur. Proc. Land. **43**(6), 1321–1334 (2018).
10. A. B. Huang, C. C. Wang, J. T. Lee, and Y. T. Ho, "Applications of FBG-based sensors to ground stability monitoring," J. Rock Mech. Geotech. Eng. **8**(4), 513–520 (2016).
11. Y. T. Ho, Y. L. Wang, L. C. Chang, T. P. Wang, and J. P. Tsai, "Optical system for monitoring groundwater pressure and temperature using fiber Bragg gratings," Opt. Express **29**(11), 16032–16045 (2021).
12. W. Q. Feng, Z. Y. Liu, H. Y. Ta, and J. H. Yin, "The pore water pressure sensor based on Sagnac interferometer with polarization-maintaining photonic crystal fiber for the geotechnical engineering," Measurement **90**, 208–214 (2016).
13. D. Inaudi, R. Walder, and R. Bulatao, "Fabry-Perot Fiber Optic Sensors for Civil and Geotechnical Monitoring of Large Structures," Struct. Health Monit. 2019.
14. A. D. Gomes, H. Bartelt, and O. Frazão, "Optical Vernier Effect: Recent Advances and Developments," Laser Photonics Rev. **15**(7), 2000588 (2021).
15. Y. Liu, X. Li, Y. N. Zhang, and Y. Zhao, "Fiber-optic sensors based on Vernier effect," Measurement **167**, 108451 (2021).
16. H. Liao, P. Lu, X. Fu, X. Jiang, W. Ni, D. Liu, and J. Zhang, "Sensitivity amplification of fiber-optic in-line Mach–Zehnder Interferometer sensors with modified Vernier-effect," Opt. Express **25**(22), 26898–26909 (2017).
17. S. Zhang, L. Yin, Y. Zhao, A. Zhou, and L. Yuan, "Bending sensor with parallel fiber Michelson interferometers based on Vernier-like effect," Opt. Laser Technol. **120**, 105679 (2019).
18. P. Robalinho, A. Gomes, and O. Frazão, "Colossal enhancement of strain sensitivity using the push-pull deformation method," IEEE Sens. J. **21**(4), 4623–4627 (2021).
19. X. Yang, S. Wu, H. Cheng, J. Ma, S. Wang, S. Liu, and P. Lu, "Simplified highly-sensitive gas pressure sensor based on harmonic Vernier effect," Opt. Laser Technol. **140**, 107007 (2021).
20. Z. Xu, Q. Sun, B. Li, Y. Luo, W. Lu, D. Liu, P. P. Shum, and L. Zhang, "Highly sensitive refractive index sensor based on cascaded microfiber knots with Vernier effect," Opt. Express **23**(5), 6662–6672 (2015).
21. Y. Jiang, Y. Yi, G. Brambilla, and P. Wang, "Ultra-high-sensitivity refractive index sensor based on dual-microfiber coupler structure with the Vernier effect," Opt. Lett. **45**(5), 1268–1271 (2020).
22. S. Wang, S. Wang, R. B. Jin, M. Feng, S. Wu, L. Zhang, and P. Lu, "All-optical demodulation fiber acoustic sensor with real-time controllable sensitivity based on optical Vernier effect," IEEE Photonics J. **11**(4), 1–11 (2019).
23. Y. Yang, Y. Wang, Y. Zhao, J. Jiang, X. He, W. Yang, Z. Zhu, W. Gao, and L. Li, "Sensitivity-enhanced temperature sensor by hybrid cascaded configuration of a Sagnac loop and a FP cavity," Opt. Express **25**(26), 33290–33296 (2017).
24. J. Li, M. Zhang, M. Wan, C. Lin, S. Huang, C. Liu, Q. He, X. Qiu, and X. Fang, "Ultrasensitive refractive index sensor based on enhanced Vernier effect through cascaded fiber core-offset pairs," Opt. Express **28**(3), 4145–4155 (2020).
25. L. Liu, T. Ning, J. Zheng, L. Pei, J. Li, J. Cao, X. Gao, and C. Zhang, "High-sensitivity strain sensor implemented by hybrid cascaded interferometers and the Vernier-effect," Opt. Laser Technol. **119**, 105591 (2019).
26. Z. Xu, Y. Luo, D. Liu, P. P. Shum, and Q. Sun, "Sensitivity-controllable refractive index sensor based on reflective θ-shaped microfiber resonator cooperated with Vernier effect," Sci. Rep. **7**(1), 1–8 (2017).
27. Q. H. Wang, X. Liu, and D. N. Wang, "Ultra-sensitive gas pressure sensor based on vernier effect with controllable amplification factor," Opt. Fiber Technol. **61**, 102404 (2021).
28. A. D. Gomes, M. S. Ferreira, J. Bierlich, J. Kobelke, M. Rothhardt, H. Bartelt, and O. Frazão, "Optical harmonic Vernier effect: A new tool for high performance interferometric fiber sensors," Sensors **19**(24), 5431 (2019).
29. A. D. Gomes, M. S. Ferreira, J. Bierlich, J. Kobelke, M. Rothhardt, H. Bartelt, and O. Frazão, "Hollow microsphere combined with optical harmonic Vernier effect for strain and temperature discrimination," Opt. Laser Technol. **127**, 106198 (2020).
30. P. M. R. Robalinho, A. D. Gomes, and O. Frazao, "High enhancement strain sensor based on Vernier effect using 2-Fiber loop mirrors," IEEE Photonics Technol. Lett. **32**(18), 1139–1142 (2020).

Optics EXPRESS

31. A. D. Gomes, J. Kobelke, J. Bierlich, J. Dellith, M. Rothhardt, H. Bartelt, and O. Frazão, "Giant refractometric sensitivity by combining extreme optical Vernier effect and modal interference," Sci. Rep. **10**(1), 1–14 (2020).
32. L. Liu, P. Lu, S. Wang, X. Fu, Y. Sun, D. Liu, J. Zhang, H. Xu, and Q. Yao, "UV adhesive diaphragm-based FPI sensor for very-low-frequency acoustic sensing," IEEE Photonics J. **8**(1), 1–9 (2016).
33. S. Wang, P. Lu, L. Liu, H. Liao, Y. Sun, W. Ni, X. Fu, X. Jiang, D. Liu, J. Zhang, H. Xu, Q. Yao, and Y. Chen, "An infrasound sensor based on extrinsic fiber-optic Fabry–Perot interferometer structure," IEEE Photonics Technol. Lett. **28**(11), 1264–1267 (2016).
34. S. Wang, W. Ni, L. Zhang, P. Lu, Y. Yang, and L. Wei, "Fiber-Based Infrasound Sensing," in *Advanced Fiber Sensing Technologies*, L. Wei, ed. (Springer, Singapore, 2020).
35. T. Nan, B. Liu, Y. Wu, J. Wang, Y. Mao, L. Zhao, T. Sun, and J. Wang, "Ultrasensitive strain sensor based on Vernier effect improved parallel structured fiber-optic Fabry-Perot interferometer," Opt. Express **27**(12), 17239–17251 (2019).
36. Y. Zhao, M. Dai, Z. Chen, X. Liu, M. S. A. Gandhi, Q. Li, and H. Y. Fu, "Ultrasensitive temperature sensor with Vernier-effect improved fiber Michelson interferometer," Opt. Express **29**(2), 1090–1101 (2021).
37. X. Zhao, Y. Zhang, W. Zhang, Z. Li, Y. Yue, and T. Yan, "Ultrasensitive Fabry–Perot Strain Sensor Based on Vernier Effect and Tapered FBG-in-Hollow Silica Tube," IEEE Sens. J. **21**(3), 3035–3041 (2021).